NANO LETTERS
Cite This: Nano Lett. 2018, 18, 3550−3556
Letter
pubs.acs.org/NanoLett

Concentration Dependence of Dopant Electronic Structure in Bottom-up Graphene Nanoribbons

Zahra Pedramrazi,[†,∞] Chen Chen,[‡,§,∞] Fangzhou Zhao,[†,§,∞] Ting Cao,[†,§] Giang D. Nguyen,[†,∥] Arash A. Omrani,[†] Hsin-Zon Tsai,[†] Ryan R. Cloke,[‡] Tomas Marangoni,[‡] Daniel J. Rizzo,[†] Trinity Joshi,[†] Christopher Bronner,[†] Won-Woo Choi,[†] Felix R. Fischer,[*,‡,§,⊥] Steven G. Louie,[*,†,§] and Michael F. Crommie[*,†,§,⊥]

[†]Department of Physics, University of California at Berkeley, Berkeley, California 94720, United States
[‡]Department of Chemistry, University of California at Berkeley, Berkeley, California 94720, United States
[§]Materials Sciences Division, Lawrence Berkeley National Laboratory, Berkeley, California 94720, United States
[∥]Center for Nanophase Materials Sciences, Oak Ridge National Laboratory, Oak Ridge, Tennessee 37831, United States
[⊥]Kavli Energy NanoSciences Institute at the University of California and Lawrence Berkeley National Laboratory, Berkeley, California 94720, United States

Supporting Information

ABSTRACT: Bottom-up fabrication techniques enable atomically precise integration of dopant atoms into the structure of graphene nanoribbons (GNRs). Such dopants exhibit perfect alignment within GNRs and behave differently from bulk semiconductor dopants. The effect of dopant concentration on the electronic structure of GNRs, however, remains unclear despite its importance in future electronics applications. Here we use scanning tunneling microscopy and first-principles calculations to investigate the electronic structure of bottom-up synthesized $N = 7$ armchair GNRs featuring varying concentrations of boron dopants. First-principles calculations of freestanding GNRs predict that the inclusion of boron atoms into a GNR backbone should induce two sharp dopant states whose energy splitting varies with dopant concentration. Scanning tunneling spectroscopy experiments, however, reveal two broad dopant states with an energy splitting greater than expected. This anomalous behavior results from an unusual hybridization between the dopant states and the Au(111) surface, with the dopant−surface interaction strength dictated by the dopant orbital symmetry.

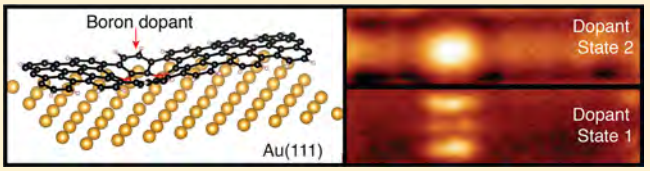

KEYWORDS: *Scanning tunneling microscopy, graphene nanoribbons, backbone boron doping, density functional theory, substrate interaction*

Quasi-one-dimensional graphene nanoribbons (GNRs) are a promising new platform for future nanoelectronics applications.[1−9] Analogous to traditional semiconductors, their electronic structure can be tailored by the introduction of heteroatom impurities.[10−14] The effect of impurity doping on GNRs, however, is not easily understood using the common framework of traditional semiconductor materials.[15,16] GNRs, for example, are intrinsically in the regime of strong quantum confinement and exhibit trigonal planar symmetry rather than the more common tetrahedral symmetry, leading to conduction through extended π-networks unlike conventional semiconducting systems. Bottom-up synthesis provides an effective method to explore heteroatom doping in GNRs since it enables site-specific incorporation of heteroatom dopants through designed precursor molecules that can be assembled into atomically precise doped GNRs.[4,17−22] The introduction of nitrogen atoms into GNR edges, for example, has been shown to shift the energy-level alignment of GNR band structure,[10,11] while the incorporation of boron atoms into the GNR backbone has been shown to introduce new in-gap states.[23−25] The electronic structure of boron-induced dopant states, however, including the effects of substrate hybridization, remains poorly understood.[21−25]

Here, we report the bottom-up synthesis and characterization of boron-doped $N = 7$ armchair GNRs (AGNRs) at two antipodal doping regimes: the dilute and highly dense limits. Scanning tunneling spectroscopy (STS) measurements and density functional theory (DFT) calculations were performed to study the local electronic properties of boron-doped GNRs in both concentration regimes. Our calculations show that there exist two boron-induced dopant states in the gap, one with s-like (even parity) and the other with p-like (odd parity) orbital character that persist in both concentration limits. In the dilute limit our freestanding calculations (i.e., no substrate coupling) show that the boron-induced dopant states are nearly degenerate. As the density of dopant atoms increases in the

Received: February 13, 2018
Revised: May 23, 2018
Published: May 31, 2018

DOI: 10.1021/acs.nanolett.8b00651
Nano Lett. 2018, 18, 3550−3556

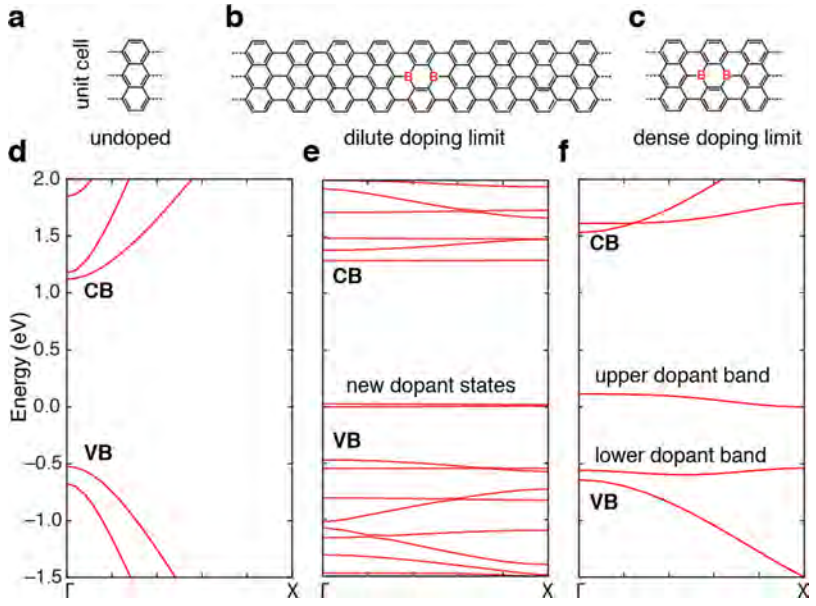

Figure 1. Band structure evolution of freestanding boron-doped $N = 7$ armchair graphene nanoribbons at different dopant densities. Unit cells of (a) undoped, (b) dilute-doped, and (c) densely doped $N = 7$ GNRs. (d–f) Corresponding band structures calculated by DFT within LDA. The relative Brillouin zone sizes in panels d, e, f are 9:1:3, and when this is taken into account, the dispersion of the VB top and CB bottom does not change significantly after doping.

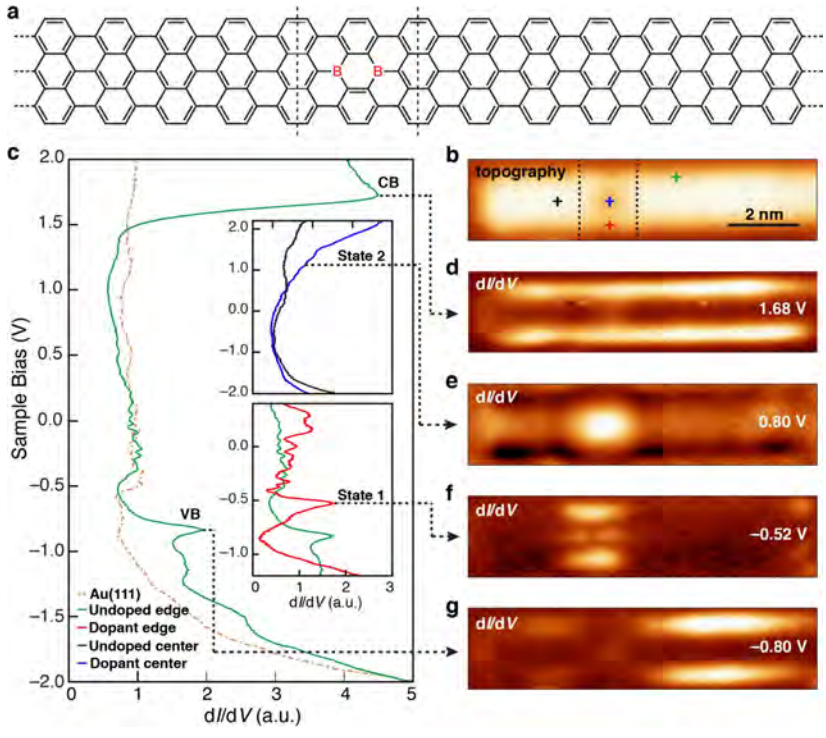

Figure 2. Electronic structure of a dilute boron-doped $N = 7$ AGNR on Au(111). (a) Wireframe sketch of a dilute-doped GNR. (b) STM topographic image of dilute-doped GNR ($V_s = -0.4$ V, $I_t = 60$ pA). (c) STM dI/dV spectroscopy measurement taken at the edge of an undoped segment of the GNR (green). Top inset shows dI/dV spectroscopy taken at the center of a boron dimer segment (blue) compared to the center of an undoped GNR segment (black). Bottom inset shows dI/dV spectroscopy taken at the edge of a boron-doped segment (red) compared to the edge of an undoped GNR segment (green). Two new states, dopant States 1 and 2, are observed at −0.52 and 0.8 eV, respectively. dI/dV maps of the GNR are shown at energies corresponding to (d) the CB edge ($V_s = 1.68$ V), (e) State 2 ($V_s = 0.8$ V), (f) State 1 ($V_s = -0.52$ V), and (g) the VB edge (the fact that the VB feature on the left side is darker is due to the asymmetrical defect placement, which likely increases quantum confinement effects on the left side) ($V_s = -0.8$ V). $T = 7$ K for all measurements. Panels d–g have the same scale as panel b.

freestanding regime, the energy separation between the boron-induced states increases, and the dopant states form impurity bands since the dopants are arranged periodically. Our experiments, however, are not consistent with the freestanding GNR predictions. In the dilute limit, we experimentally observe two dopant states with different symmetries that are strongly

DOI: 10.1021/acs.nanolett.8b00651
Nano Lett. 2018, 18, 3550–3556

split in energy and broadened into asymmetric peaks (i.e., one is broader than the other). In the dense limit, the experimental upper dopant energy band is shifted in energy with respect to the freestanding theoretical prediction and is significantly broader than expected. This anomalous behavior is explained by hybridization between the boron-induced dopant states and the surface states of the gold substrate. First-principles calculations taking substrate coupling into account confirm that there is a strong and symmetry-dependent hybridization between GNR dopant states and Au(111). Consequently, as seen experimentally, this induces strong energy splitting and asymmetrical broadening whose magnitude depends on the dopant state symmetry.

Results. Figure 1 shows a DFT calculation (using the local density approximation (LDA)) of the electronic structure of a freestanding $N = 7$ AGNR (i.e., no substrate included in the calculation) for three boron dopant concentrations: (i) the undoped case (Figure 1d), (ii) the dilute doping limit (Figure 1e), and (iii) the dense doping limit (Figure 1f) (Figures 1a−c show the unit cells used for the three calculations). GW[26−28] calculations were seen to give similar results but with larger bandgap values due to self-energy effects. We focus here on the DFT results since substrate screening typically reduces the GW bandgaps to values close to the DFT level when the system is put on a metallic surface (as done in our experiments). The undoped GNR band structure shows the familiar conduction (CB) and valence (VB) bands that have been calculated within DFT before,[29] while the dilute-doped GNR exhibits band edges at similar energies. The most significant difference between the undoped and dilute-doped band structure is the presence of two new defect levels at ∼0.5 eV above the VB edge for the dilute-doped case (the appearance of multiple bands above (below) the conduction (valence) band edge for the dilute-doped limit is due to band-folding from the supercell geometry used in the calculation). The new impurity states are nearly degenerate (ΔE < 20 meV) and exhibit a large contribution from the π-orbitals of the boron dopant atoms. Analysis of the wave function for the lower defect state shows that it has *p*-like symmetry (odd parity) along the GNR axial direction (Figure S1cb in the Supporting Information (SI)), while the upper defect state has *s*-like symmetry (even parity) along the longitudinal axis (Figure S1c) (a similar theoretical result for the dilute, freestanding limit was reported in ref 25). As the dopant concentration increases, the energy splitting between the two impurity states correspondingly increases, and the defect states evolve into impurity bands with an energy gap of 0.5 eV, as shown in the band structure for the densely doped GNR in Figure 1f (Figure S2 in the SI shows the calculated band structures for other intermediate dopant densities) (the band labeling convention used here is different compared to a previous publication[23] in order to make the role of the dopants more clear).

In order to experimentally test these theoretical predictions, GNRs were fabricated in both the dilute and dense regimes. The dilute-doped regime was accessed by combining molecular precursors for undoped $N = 7$ GNR (10,10′-dibromo-9,9′-bianthryl, DBBA) with precursors for boron-doped $N = 7$ AGNR (see Figure S4 of the SI) in a 10:1 ratio using standard GNR growth conditions[4,18,19] (polymerization of the precursors occurs at ∼180 °C, while cyclodehydrogenation occurs at ∼360 °C (see Methods)). Figure 2b shows an STM topographic image of a resulting dilute-doped $N = 7$ GNR on Au(111) with vertical dashed lines indicating the location of a boron defect (a sketch of the wireframe structure is shown in Figure 2a). The region surrounding the dopant atoms has a reduced apparent height in the STM image, suggesting that the boron atoms sit closer to the Au(111) surface than the GNR carbon atoms.

The experimental electronic structure of dilute-doped GNRs was investigated by measuring STM differential conductance (dI/dV) spectra at the position of boron dopants and then comparing that to spectra acquired on undoped GNR segments at the positions marked in Figure 2b (the respective positions are color-coded with the dI/dV curves). Figure 2c shows a characteristic dI/dV point spectrum (green curve) recorded at the edge of an undoped segment of the GNR. This spectrum exhibits a peak at $V_s = 1.68 \pm 0.02$ V, which we identify as the CB edge, as well as a peak at $V_s = -0.80 \pm 0.02$ V, which is identified as the VB edge (V_s is sample voltage). This leads to an overall GNR bandgap of 2.48 ± 0.02 eV, similar to bandgap measurements on undoped $N = 7$ AGNRs performed previously.[26,29,30] The identity of these familiar spectroscopic peaks was confirmed via energy-resolved dI/dV mapping, which allows visualization of the surface local density of states (LDOS) as depicted in Figure 2d−g. Two new states attributed to the dopant atoms are observed in the STM spectroscopy measured at the center (top inset of Figure 2c, blue curve) and edge (bottom inset of Figure 2c, red curve) of the boron defect shown in Figure 2b. The dI/dV spectrum measured at the impurity edge (red curve) shows the presence of a new peak (labeled State 1) that is centered at $V_s = -0.52 \pm 0.02$ V and that has a full width at half-maximum (fwhm) of 0.23 V. The dI/dV spectrum measured at the center of the dopant site (blue curve) exhibits a pronounced upward slope starting at $V_s \approx 0.3$ V and extending to $V_s \approx 1.2$ V that is not observed in the reference spectrum taken at the center of the undoped segment with the same tip (black curve). This second dopant-induced feature is labeled as State 2. We note that these spectroscopic features (States 1 and 2) persist even as adjacent dopants in the dilute regime have interimpurity distances as small as 2.5 nm center-to-center (see SI Figure S3).

The spatial distributions of dopant-induced States 1 and 2 were determined using dI/dV mapping. Figure 2f shows a dI/dV map measured at the energy of State 1 that exhibits bright lines along the edges of the dopant segment as well as two small high intensity spots near the boron atoms (the two central bright spots are located at the sites of the two horizontal boron−carbon bonds, see Figure S8). Figure 2e shows a representative dI/dV map of State 2 recorded at 0.8 V that exhibits bright, diffuse LDOS that is elliptically symmetric and centered at the position of the dopant (dI/dV maps recorded for State 2 at different energies in the range 0.3 V < V_s < 1.35 V show similar LDOS patterns, see SI Figure S6).

We next explored GNRs doped with boron atoms in the dense limit. These GNRs were grown using only the boron-doped precursor (Figure S4b). A wireframe sketch of the resulting boron-doped GNR structure is depicted in Figure 3a, and an STM topograph is shown in Figure 3b. As seen previously,[23,24] the boron-doped segments of this GNR sit slightly closer to the substrate than the unsubstituted regions and lead to a 1.30 ± 0.05 Å amplitude periodic height modulation along the GNR long axis in topography. We first characterized the electronic structure of densely doped GNRs via dI/dV point spectroscopy. Figure 3c shows typical dI/dV spectra measured at a position along the backbone (blue curve) and at the edge (red curve) of a densely doped GNR with the

DOI: 10.1021/acs.nanolett.8b00651
Nano Lett. 2018, 18, 3550−3556

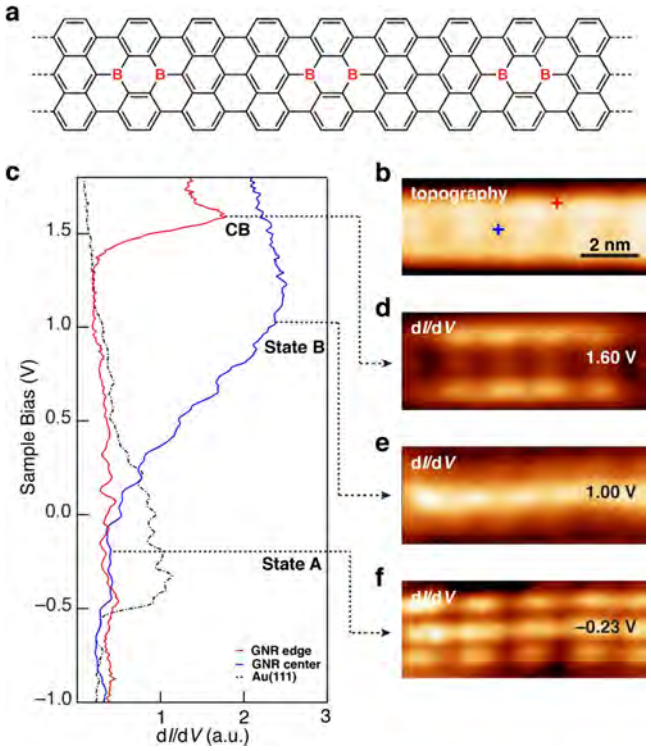

Figure 3. Electronic structure of densely boron-doped $N = 7$ AGNR on Au(111). (a) Wireframe sketch of a densely doped GNR. (b) STM topograph parameters: V_s = 1.60 V, I_t = 20 pA. (c) STM dI/dV spectroscopy measured at the edge and center of a densely doped GNR as shown in panel b. (d) dI/dV map taken at V_s = 1.60 V visualizes state at the CB edge. (e) dI/dV map taken at V_s = 1.0 V visualizes unoccupied dopant-induced state (State B). (f) dI/dV map taken at V_s = −0.23 V visualizes occupied dopant-induced state (State A). T = 4.5 K for all measurements. Panels d−f have the same scale as panel b.

same tip (spectroscopy positions are marked in Figure 3b; the spectroscopic features had no significant dependence on how the tip was axially aligned with respect to dopants (see Figure S11)). The dI/dV spectrum recorded at the GNR edge shows a well-defined peak at 1.63 ± 0.04 eV above the Fermi level, E_F.[24] The spectrum recorded along the densely doped GNR backbone is quite different and reveals a new, broad spectroscopic feature at 1.0 ± 0.2 eV above E_F (this peak is absent in STS of undoped GNRs[29−31]). We did not observe any reproducible spectroscopic features below E_F in our dI/dV point spectra for densely doped GNRs on Au(111).

We used dI/dV mapping to visualize the electronic structure of densely doped GNRs at different energies. Figure 3d shows a dI/dV map recorded at 1.60 eV, the energy of the upper spectroscopic peak. Here, the intensity of the LDOS is highest along the GNR edges, similar to what has previously been observed for energies near the CB edge in undoped $N = 7$ AGNRs.[24,26,29,30] The dI/dV map obtained at an energy near the broad spectroscopic peak at 1.0 eV shows a pronounced shift in LDOS away from the GNR edges to the GNR backbone (Figure 3e). Figure 3f shows a dI/dV map obtained in the filled states at a voltage of V_s = −0.23 V. Although we observe no peak at this energy in the dI/dV point spectroscopy, a clear transition is observed in the spatial LDOS distribution compared to dI/dV maps obtained at higher voltages (see Figure S10 in the SI). At this filled state energy, the LDOS is pushed outward toward the GNR edges, and a longitudinal nodal structure is seen that does not appear in the map at V_s = 1.0 V. The new densely doped spectroscopic features observed at V_S = −0.23 and 1.0 V do not occur for undoped $N = 7$ GNRs and so must arise from the influence of boron dopants. We label them here as State A (V_S = −0.23 V) and State B (V_S = 1.0 V).

Our experimental results for dilute and densely doped GNRs exhibit some qualitative agreement with our theoretical calculations for freestanding boron-doped GNRs, but there are significant discrepancies. For example, in the dilute-doping limit, our experiments faithfully reproduce the two expected defect states in the gap with one exhibiting *s*-like symmetry (State 2, which has no node) and the other exhibiting *p*-like symmetry (State 1, which has a node). However, our experimental measurements show a significant splitting between the two states (∼1 eV), whereas the theoretical defect states are essentially degenerate. Furthermore, it is not clear why the experimental peak seen for State 1 is so much narrower than the broad, sloping spectroscopic feature that defines State 2.

In the densely doped regime, the experimental peak observed at V_s = 1.6 eV (Figure 3c, red curve) is consistent with the theoretically predicted CB (Figure 1f). The new spectroscopic peak at $V_s \approx$ 1.0 V (Figure 3c, blue curve) also roughly corresponds to spectroscopic features expected to arise from a new dopant-induced band[25] (e.g., the upper dopant band in Figure 1f). However, there are major discrepancies between experiment and theory here as well. Most significant is the energy alignment of the observed spectroscopic features. The energy difference between the two experimental spectroscopic peaks shown in Figure 3c is only ∼0.5 eV, whereas the theoretically predicted energy difference between the CB and the upper dopant band in Figure 1f is ∼1.5 eV. Also, if the state imaged at V = −0.23 eV (Figure 3f) is assigned to the lower dopant band, then the energy difference between the two dopant-induced bands in the experiment (∼1.2 eV) is significantly larger than the calculated energy difference (0.5 eV). Moreover, the anomalously broad spectroscopic peak at V_s = 1.0 V is inconsistent with the simulation since the upper dopant bandwidth is predicted to be quite narrow (Figure 1f).

We conclude that the freestanding GNR model used in the calculations is insufficient to describe our experimental data, most likely because it neglects the substrate. Therefore, in order to better understand our experimental results, we performed additional calculations that fully take into account coupling from the underlying Au(111) substrate upon which the boron-doped GNRs rest. The electronic structures of both dilute-doped and densely doped GNRs on Au(111) were calculated via DFT using the supercells shown in Figures 4d and 5d, respectively. Similar to our experimental data, the boron atoms in a fully relaxed simulated GNR sit closer to the Au(111) surface than the carbon atoms in undoped segments of the ribbon. This reduction of the boron−gold distance indicates significant interaction between the boron dopants and the gold substrate atoms.

In order to simulate the dilute-doped dI/dV spectroscopy of Figure 2c, we calculated the energy-resolved local density of states (LDOS) (including gold substrate effects) averaged over a 7.5 Å × 7.5 Å area 4 Å above the boron-doped segment following the topography of the GNR. The results are plotted in Figure 4a. Substantial features are seen to appear in previously gapped regions due to hybridization between the GNR and the underlying Au(111) substrate (the CB (1.6 eV)

DOI: 10.1021/acs.nanolett.8b00651
Nano Lett. 2018, 18, 3550−3556

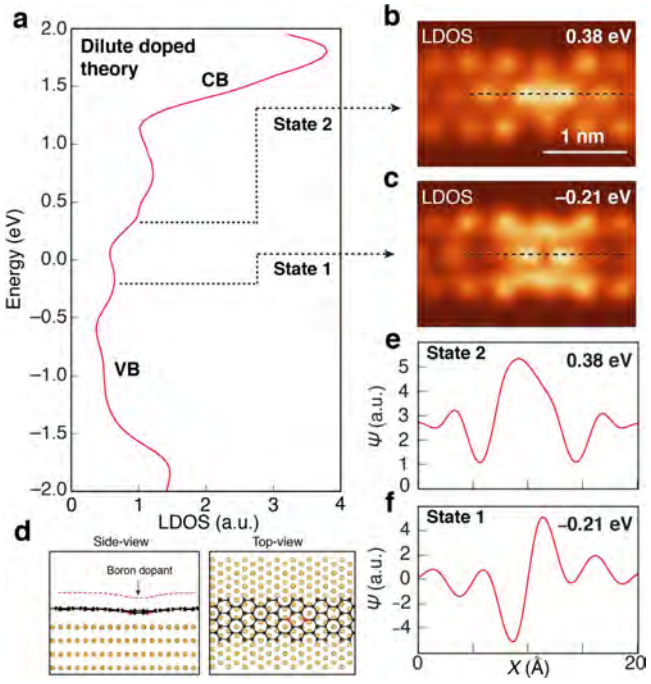

Figure 4. DFT-LDA calculation of dilute-doped N = 7 GNR on Au(111) substrate. (a) Calculated LDOS 4 Å above the boron-doped segment shows dopant States 1 and 2 (theoretical LDOS is broadened by a Gaussian function with standard deviation σ = 125 meV). Calculated LDOS map is shown for (b) E = 0.38 eV (integrated over a 0.05 eV energy window) and (c) E = −0.21 eV (integrated over a 0.05 eV energy window). (d) Side-view and top-view of the supercell and the relaxed structure used to calculate the dilute-doped GNR. The supercell includes four layers of Au atoms. Red dashed line shows the surface upon which the LDOS maps are calculated. (e) Calculated wave function along the dashed line in panel b for E = 0.38 eV. (f) Calculated wave function along the dashed line in panel c for E = −0.21 eV. Panels b and c have the same scale.

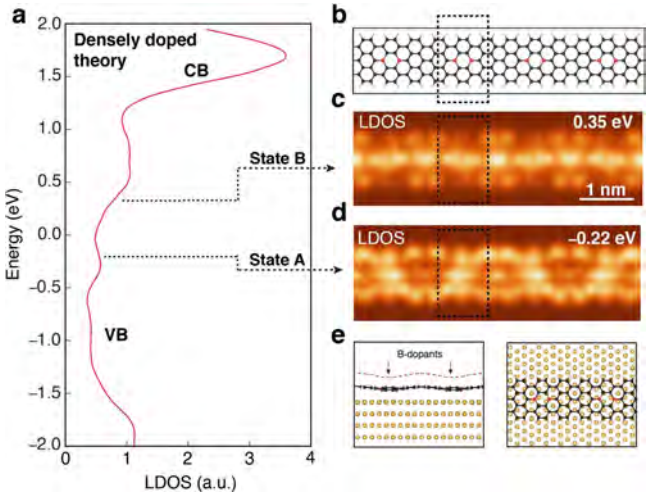

Figure 5. DFT-LDA calculation of densely doped N = 7 GNR on Au(111) substrate. (a) Calculated LDOS 4 Å above boron-doped segment shows dopant States A and B (theoretical LDOS is broadened by a Gaussian function with standard deviation σ = 125 meV). (b) Wireframe sketch shows location of boron atoms. Calculated LDOS maps (each including four boron dimers) are shown for (c) E = 0.35 eV (integrated over a 0.05 eV energy window) and (d) E = −0.22 eV (integrated over a 0.05 eV energy window). (e) Side view and top view of the supercell and the relaxed structure (includes four layers of Au atoms) used to calculate the relaxed densely doped GNR. The red dashed line shows the surface upon which the LDOS maps are calculated. Panels c and d have the same scale.

and VB (−0.9 eV) edges are obtained from the undoped segment as explained in the SI). In particular, two features are observed that arise from the boron defect: a broad resonance in the unoccupied states and a narrower resonance in the occupied states. The occupied resonance appears in the range −0.4 eV < E < −0.1 eV and exhibits the LDOS pattern shown in Figure 4c (obtained at E = −0.21 eV). This LDOS map has bright features at the outer edges and two interior peaks of high intensity located on the C−B bonds that lie along the GNR axis. As seen in Figure 4f, the wave function at this energy has odd parity (p-like) under mirror symmetry.

The unoccupied LDOS is quite different from what is seen in the occupied states. Here a much broader feature arises over the range 0.3 eV < E < 0.9 eV (a slight dip can be seen at $E \approx$ 0.5 eV). Figure 4b shows a representative LDOS map of this defect state (obtained at E = 0.38 eV). As seen in Figure 4e, this dopant state has a more delocalized wave function than the occupied state feature and exhibits approximate even parity (s-like).

The simulated behavior of the dilute-doped GNR on Au(111) supports our hypothesis that differences observed between the experiment and the "freestanding" theory arise from the interaction between boron-doped GNRs and the gold substrate. The reasonably good agreement between theory and experiment for the defect state energies and broadening allows us to identify the occupied and unoccupied features in the theoretical LDOS of Figure 4a with experimentally observed State 1 and State 2 of Figure 2c. Further evidence for this assignment is found in the striking resemblance of the theoretical occupied state LDOS pattern (Figure 4c) to State 1 (Figure 2f), as well as the resemblance of the theoretical unoccupied LDOS pattern (Figure 4b) to State 2 (Figure 2e). The energy splitting between the central energy of the two simulated defect state peaks (∼1 V) is also similar to what is observed experimentally, indicating that the boron-induced defect states (which are nearly degenerate for a freestanding GNR) are strongly split by interaction with the Au(111) substrate. This interaction also explains the different broadening of the two defect states, which is faithfully reproduced by the calculation and which arises due to the different symmetries of the dopant states. Because State 1 has p-like character, it hybridizes more weakly with the s-like surface states of gold (leading to a narrower peak), whereas State 2 has s-like character and so hybridizes more strongly with gold (leading to a broader peak). The s- and p-like symmetries of the boron defect states are thus primary factors in determining the dopant electronic structure for the strongly hybridized boron-doped GNR/Au(111) complex.

Motivated by the agreement between experiment and theory for the dilute-doped GNRs in the presence of Au(111), we examined the electronic structure of densely doped GNRs supported by Au(111). The energy-resolved LDOS 4 Å above the boron-doped segment was calculated using the same method as in the dilute case and is shown in Figure 5a. The energy-dependent LDOS of Figure 5a is very similar to what is seen in the dilute-doped case (Figure 4a). For example, a broad unoccupied resonance and a narrower occupied resonance arise due to substrate interactions, and the resonances have almost identical energy and width as the State 1 and 2 features of the

DOI: 10.1021/acs.nanolett.8b00651
Nano Lett. 2018, 18, 3550−3556

dilute regime. A representative LDOS map of the theoretical unoccupied states obtained at E = 0.35 eV (Figure 5c) is dominated by nearly uniform bright intensity along the longitudinal axis of the densely doped GNR (i.e., bright intensity occurs at the boron dimer sites as well as at the carbon dimer sites between them). This theoretical LDOS map is qualitatively very similar to the experimental unoccupied state dI/dV map of Figure 3e, and so we identify the broad, unoccupied state feature of Figure 5a as State B. A representative map of the theoretical occupied states obtained at E = −0.22 eV (Figure 5d) shows a shifting of LDOS intensity to the GNR edges and a new lateral periodicity whose wavelength matches the distance between boron dimers (due to reduction in LDOS at the carbon dimer sites between boron dimers). This theoretical LDOS map is qualitatively similar to the experimental occupied state dI/dV map of Figure 3f, and so we identify the narrow, occupied state feature of Figure 5a as State A. The lack of a clear peak due to State A in the experimental dI/dV point spectroscopy (Figure 3c) is likely due to increased hybridization between densely doped lower dopant band states and the Au(111) surface compared to dopant states in the dilute-doped regime.

Our simulations allow us to confirm that the underlying physics determining the behavior of densely doped GNRs is similar to the symmetry-dependent mechanism at work in the dilute-doped regime, despite the significant difference in dopant concentrations. This can be seen by examining the wave functions of occupied and empty states for densely doped GNRs (Figure S12, SI). The wave function for State B is seen to be symmetric around a line bisecting a boron dimer and thus exhibits s-like symmetry similar to State 2 of the dilute regime (Figure 4e). This explains why the densely doped GNR couples so strongly to the s-like conduction band of Au(111) at this energy, thus leading to the broad, unoccupied resonance observed both theoretically (Figure 5a) and experimentally (Figure 3c), which looks so similar to State 2 of the dilute regime. The wave function for State A, however, has p-like symmetry around the boron dimer (Figure S12b, SI) which explains why it couples less strongly to the gold conduction band and exhibits a narrower resonance, similar to State 1 of the dilute regime. Due to the dominant effects of substrate hybridization, States A and B of the dense regime can be heuristically thought of as simple 1D arrays of States 1 and 2 of the dilute regime, respectively. Despite this strong substrate interaction, however, states A and B can still be associated with the lower and upper dopant bands of the freestanding GNR shown in Figure 1f. The experimental energies of these states can thus be used to extract an apparent bandgap of $E_g \approx 1.2$ eV for densely doped GNRs on Au(111).

In conclusion, our experimental and theoretical studies show that introduction of boron dopants into AGNRs induces the formation of two new in-gap dopant states that have different symmetries. These dopant-induced states continuously evolve as the boron dopant concentration increases. Moreover, we see that hybridization between dopant atoms and the underlying Au(111) substrate has an unusually strong impact on the electronic structure of boron-doped GNRs, much greater than for other doped GNR systems studied to date.[10,11,32] Both the dilute and densely doped electronic behavior depends strongly on the impurity state symmetry, with s-like (p-like) states hybridizing more strongly (weakly) with the gold substrate, thus leading to strong, symmetry-dependent energy splitting. This strong substrate coupling masks the effects of impurity−impurity interactions that are predicted for freestanding boron-doped GNRs. We thus expect very different electronic behavior (including a clearer, more well-defined bandgap) for boron-doped GNRs placed on substrates that interact less strongly with boron impurity atoms than gold.

Methods. All STM and STS measurements were performed at T = ∼7 K. Molecular precursors for bottom-up synthesized GNRs were deposited onto clean Au(111) single crystal surfaces held at 24 °C. Subsequent to deposition, the sample was annealed to 640 K over 30 min and held at that temperature for 40 min to induce the polymerization and cyclodehydrogenation necessary to form boron-doped GNRs. The spectroscopic features reported here (including dI/dV maps) were consistently observed on 13 different dilute-doped GNRs and 11 different densely doped GNRs whose electronic properties were inspected using a variety of different STM tips. All STM topographic images were processed using WSxM.[33]

First-principles calculations were performed using DFT in the local density approximation, implemented in the Quantum Espresso[34] package. We used ultrasoft pseudopotentials with a plane-wave energy cutoff of 40 Ry to calculate freestanding boron-doped GNRs as well as boron-doped GNRs on Au(111). Dangling bonds were capped by hydrogen, and all structures were fully relaxed until the force on each atom was less than 0.02 eV Å^{-1}. For calculations that included a gold substrate, the GNR was positioned on top of a Au(111) surface that included 288 gold atoms in four layers within the supercell. The GNR was placed perpendicular to the Au(110) crystallographic direction to ensure commensuration between the unit cell of gold and the GNR to within less than 1% lattice mismatch. The GNR was slightly strained initially to fit the lattice constant of gold but was then fully relaxed until the forces on every atom were less than 0.02 eV Å^{-1}. GW calculations were performed using the BerkeleyGW package.[35]

■ ASSOCIATED CONTENT

Supporting Information

The Supporting Information is available free of charge on the ACS Publications website at DOI: 10.1021/acs.nanolett.8b00651.

Symmetry calculation on freestanding dilute doped ribbon, intermediate dopant concentration, chemical structure of the ribbons, large-scale image, detailed electronic structure of the dopant states, discussion of conduction and valence bands, comparison of dI/dV spectroscopies in densely doped AGNR, calculated wave functions in densely doped AGNR, tight-binding theory for b-doped GNRs (PDF)

■ AUTHOR INFORMATION

Corresponding Authors

*E-mail: crommie@berkeley.edu.
*E-mail: sglouie@berkeley.edu.
*E-mail: ffischer@berkeley.edu.

ORCID

Trinity Joshi: 0000-0001-7566-3528
Christopher Bronner: 0000-0002-0083-5089
Felix R. Fischer: 0000-0003-4723-3111
Steven G. Louie: 0000-0003-0622-0170
Michael F. Crommie: 0000-0001-8246-3444

DOI: 10.1021/acs.nanolett.8b00651
Nano Lett. 2018, 18, 3550−3556

Author Contributions

[∞]Z.P., C.C. and F.Z. contributed equally to this work. Z.P., C.C., G.D.N., A.A.O., H.T., D.J.R., T.J., C.B., W.C., and M.F.C. performed STM measurements and analyzed STM data. F.Z., T.C., and S.G.L. carried out GNR calculations and interpretation of STM data. R.R.C., T.M., and F.R.F. synthesized the precursor molecules. All authors discussed and wrote the paper.

Notes

The authors declare no competing financial interest.

■ ACKNOWLEDGMENTS

Research supported by the U.S. Department of Energy (DOE), Office of Science, Basic Energy Sciences (BES), under Award No. DE-SC0010409 (design of molecular building blocks) and Nanomachine Program award no. DE-AC02-05CH11231 (surface reaction characterization and DFT calculations), by the Office of Naval Research BRC Program (precursor synthesis, GNR imaging), by DARPA, the U.S. Army Research Laboratory and the U.S. Army Research Office under Contract/Grant No. W911NF-15-1-0237 (spectroscopy), and by the National Science Foundation under Grant No. DMR-1508412 and the NSF Center for Energy Efficient Electronics Science (E3S, NSF Grant No. ECCS-0939514) (development of theory formalism and tight-binding analyses). Computational resources have been provided by the DOE at Lawrence Berkeley National Laboratory's NERSC facility. C.B. acknowledges support through the Fellowship Program of the German National Academy of Sciences Leopoldina under Grant No. LPDS 2014-09. T.J. acknowledges support from NSF Graduate Research Fellowship Program under Grant No. DGE 1106400.

■ REFERENCES

(1) Shen, Y.-T.; Deng, K.; Zhang, X.; Feng, W.; Zeng, Q.; Wang, C.; Gong, J. *Nano Lett.* **2011**, *11*, 3245−3250.
(2) Son, Y.-W.; Cohen, M. L.; Louie, S. G. *Nature* **2006**, *444*, 347−349.
(3) Bennett, P. B.; Pedramrazi, Z.; Madani, A.; Chen, Y.-C.; de Oteyza, D. G.; Chen, C.; Fischer, F. R.; Crommie, M. F.; Bokor, J. *Appl. Phys. Lett.* **2013**, *103*, 253114.
(4) Cai, J.; Ruffieux, P.; Jaafar, R.; Bieri, M.; Braun, T.; Blankenburg, S.; Muoth, M.; Seitsonen, A. P.; Saleh, M.; Feng, X.; Müllen, K.; Fasel, R. *Nature* **2010**, *466*, 470−473.
(5) Han, M. Y.; Özyilmaz, B.; Zhang, Y.; Kim, P. *Phys. Rev. Lett.* **2007**, *98*, 206805.
(6) Kim, W. Y.; Kim, K. S. *Nat. Nanotechnol.* **2008**, *3*, 408−412.
(7) Yang, L.; Park, C.-H.; Son, Y.-W.; Cohen, M. L.; Louie, S. G. *Phys. Rev. Lett.* **2007**, *99*, 186801.
(8) Yan, Q.; Huang, B.; Yu, J.; Zheng, F.; Zang, J.; Wu, J.; Gu, B.; Liu, F.; Duan, W. *Nano Lett.* **2007**, *7*, 1469−1473.
(9) Wang, X.; Ouyang, Y.; Li, X.; Wang, H.; Guo, J.; Dai, H. *Phys. Rev. Lett.* **2008**, *100*, 206803.
(10) Bronner, C.; Stremlau, S.; Gille, M.; Brauße, F.; Haase, A.; Hecht, S.; Tegeder, P. *Angew. Chem., Int. Ed.* **2013**, *52*, 4422−4425.
(11) Cai, J.; Pignedoli, C. A.; Talirz, L.; Ruffieux, P.; Söde, H.; Liang, L.; Meunier, V.; Berger, R.; Li, R.; Feng, X.; Müllen, K.; Fasel, R. *Nat. Nanotechnol.* **2014**, *9*, 896−900.
(12) Martins, T. B.; Miwa, R. H.; da Silva, A. J. R.; Fazzio, A. *Phys. Rev. Lett.* **2007**, *98*, 196803.
(13) Li, Y.; Zhou, Z.; Shen, P.; Chen, Z. *ACS Nano* **2009**, *3*, 1952−1958.
(14) Terrones, H.; Lv, R.; Terrones, M.; Dresselhaus, M. S. *Rep. Prog. Phys.* **2012**, *75*, 062501.
(15) Cervantes-Sodi, F.; Csányi, G.; Piscanec, S.; Ferrari, A. C. *Phys. Rev. B.* **2008**, *77*, 165427.
(16) Biel, B.; Blase, X.; Triozon, F.; Roche, S. *Phys. Rev. Lett.* **2009**, *102*, 096803.
(17) Nguyen, G. D.; Toma, F. M.; Cao, T.; Pedramrazi, Z.; Chen, C.; Rizzo, D. J.; Joshi, T.; Bronner, C.; Chen, Y.-C; Favaro, M.; Louie, S. G.; Fischer, F. R.; Crommie, M. F. *J. Phys. Chem. C* **2016**, *120*, 2684−2687.
(18) Chen, Y.-C.; de Oteyza, D. G.; Pedramrazi, Z.; Chen, C.; Fischer, F. R.; Crommie, M. F. *ACS Nano* **2013**, *7*, 6123−6128.
(19) van der Lit, J.; Boneschanscher, M. P.; Vanmaekelbergh, D.; Ijäs, M.; Uppstu, A.; Ervasti, M.; Harju, A.; Liljeroth, P.; Swart, I. *Nat. Commun.* **2013**, *4*, 2023.
(20) Ruffieux, P.; Wang, S.; Yang, B.; Sánchez-Sánchez, C.; Liu, J.; Dienel, T.; Talirz, L.; Shinde, P.; Pignedoli, C. A.; Passerone, D.; Dumslaff, T.; Feng, X.; Müllen, K.; Fasel, R. *Nature* **2016**, *531*, 489−492.
(21) Talirz, L.; Söde, H.; Dumslaff, T.; Wang, S.; Sanchez-Valencia, J.; Liu, J.; Shinde, P.; Pignedoli, C. A.; Liang, L.; Meunier, V.; Plumb, N. C.; Shi, M.; Feng, X.; Narita, A.; Müllen, K.; Fasel, R.; Ruffieux, P. *ACS Nano* **2017**, *11*, 1380−1388.
(22) Zhang, H.; Lin, H.; Sun, K.; Chen, L.; Zagranyarski, Y.; Aghdassi, N.; Duhm, S.; Li, Q.; Zhong, D.; Li, Y.; Müllen, K.; Fuchs, H.; Chi, L. *J. Am. Chem. Soc.* **2015**, *137*, 4022−4025.
(23) Cloke, R. R.; Marangoni, T.; Nguyen, G. D.; Joshi, T.; Rizzo, D. J.; Bronner, C.; Cao, T.; Louie, S. G.; Crommie, M. F.; Fischer, F. R. *J. Am. Chem. Soc.* **2015**, *137*, 8872−8875.
(24) Kawai, S.; Saito, S.; Osumi, S.; Yamaguchi, S.; Foster, A. S.; Spijker, P.; Meyer, E. *Nat. Commun.* **2015**, *6*, 8098.
(25) Carbonell-Sanromà, E.; Brandimarte, P.; Balog, R.; Corso, M.; Kawai, S.; Garcia-Lekue, A.; Saito, S.; Yamaguchi, S.; Meyer, E.; Sánchez-Portal, D.; Pascual, J. I. *Nano Lett.* **2017**, *17*, 50−56.
(26) Chen, Y.-C.; Cao, T.; Chen, C.; Pedramrazi, Z.; Haberer, D.; de Oteyza, D. G.; Fischer, F. R.; Louie, S. G.; Crommie, M. F. *Nat. Nanotechnol.* **2015**, *10*, 156−160.
(27) Hybertsen, M. S.; Louie, S. G. *Phys. Rev. B.* **1986**, *34*, 5390−5413.
(28) Cao, T.; Zhao, F.; Louie, S. G. *Phys. Rev. Lett.* **2017**, *119*, 076401.
(29) Ruffieux, P.; Cai, J.; Plumb, N. C.; Patthey, L.; Prezzi, D.; Ferretti, A.; Molinari, E.; Feng, X.; Müllen, K.; Pignedoli, C. A.; Fasel, R. *ACS Nano* **2012**, *6*, 6930−6935.
(30) Koch, M.; Ample, F.; Joachim, C.; Grill, L. *Nat. Nanotechnol.* **2012**, *7*, 713−717.
(31) Ijäs, M.; Ervasti, M.; Uppstu, A.; Liljeroth, P.; van der Lit, J.; Swart, I.; Harju, A. *Phys. Rev. B.* **2013**, *88*, 075429.
(32) Nguyen, G. D.; Tsai, H. Z.; Omrani, A. A.; Marangoni, T.; Wu, M.; Rizzo, D. J.; Rodgers, G. F.; Cloke, R. R.; Durr, R. A.; Sakai, Y.; Liou, F.; Aikawa, A. S.; Chelikowsky, J. R.; Louie, S. G.; Fischer, F. R.; Crommie, M. F. *Nat. Nanotechnol.* **2017**, *12*, 1077.
(33) Horcas, I.; Fernández, R. *Rev. Sci. Instrum.* **2007**, *78*, 013705.
(34) Giannozzi, P.; Baroni, S.; Bonini, N.; Calandra, M.; Car, R.; Cavazzoni, C.; Ceresoli, D.; Chiarotti, G. L.; Cococcioni, M.; Dabo, I. *J. Phys.: Condens. Matter* **2009**, *21*, 395502.
(35) Deslippe, J.; Samsonidze, G.; Strubbe, D. A.; Jain, M.; Cohen, M. L.; Louie, S. G. *Comput. Phys. Commun.* **2012**, *183*, 1269−1289.

DOI: 10.1021/acs.nanolett.8b00651
Nano Lett. 2018, 18, 3550−3556